Dalton Transactions

ROYAL SOCIETY OF CHEMISTRY

www.rsc.org/dalton

Mechanical preparation of nanocrystalline biocompatible single phase Mn doped A-type carbonated hydroxyapatite (A-cHAp): Effect of Mn doping on microstructure

S. Lala[a], M. Ghosh[b], P.K. Das [b], T. Kar[c], S. K. Pradhan[a*1]

[a] *Materials Science Division, Department of Physics, The University of Burdwan, Golapbag, Burdwan-713104, West Bengal, India*
[b] *Department of Biological Chemistry, Indian Association for the Cultivation of Science, Jadavpur, Kolkata – 700 032, India*
[c] *Department of Materials Science, Indian Association for the Cultivation of Science, Jadavpur, Kolkata-700032, India*

Abstract

Nanocrystalline biocompatible single phase Mn doped A-type carbonated hydroxyapatite (A-cHAp) powder has been synthesized by mechanical alloying the stoichiometric mixture of $CaCO_3$, $CaHPO_4.2H_2O$ and MnO powder for 10h at room temperature under open air. The A-type carbonation in HAp (substitution of CO_3^{2-} for OH^-) is confirmed by FTIR analysis. Microstructure characterization in terms of lattice imperfections and phase quantification of ball milled samples are made by analyzing XRD patterns employing Rietveld's structure refinement method. Rietveld analysis of XRD patterns recorded from Mn-doped HAp samples has been used to locate Mn^{2+} cations in HAp. The Ca2 vacancy site is found to be more favorable for Mn substitution. Microstructure characterization by HRTEM corroborates the findings of the x-ray analysis where the presence of significant amount of amorphous phase of HAp analogous to indigenous bone mineral is clearly found. MTT assay shows sufficiently high percentage cell viability confirming the cytocompatibility of the sample.

---

*Corresponding author
E-mail: skpradhan@phys.buruniv.ac.in; FAX :+91 342 2530452

Introduction

The hard tissues in native bone are composed of calcium phosphate minerals combined with collagen fibrils providing stiffness, strength and toughness to bone. [1, 2] The inorganic phosphate minerals support the body mechanically and store and release calcium and other ions into body fluid to maintain homeostasis. [3] Hydroxyapatite (HAp) with chemical formula $Ca_{10}(PO_4)_6(OH)_2$ is the main mineral component of the inorganic part of bone. HAp has been a novel bioceramic in orthopedic surgery of damaged bone and teeth due to its excellent biocompatibility, bioactivity and osteoconductivity. [4-6] However, the apatites found in native bone have chemical composition very complicated and it differs from pure HAp primarily owing to its non-stoichiometric composition and calcium deficient environment (Ca/P molar ratio < 1.67) due to presence of different cations and anions such as Na^+, Zn^{2+}, Mg^{2+}, Mn^{2+}, CO_3^{2-}, F^- etc. [1,7] These ions are taken up from body fluids during bone metabolism controlling solubility and osteoconductivity of bone minerals. [3] Bone mineral contains about 2-8% carbonate [1, 8, 9] depending upon the age. [10] There exists two types of carbonated apatite in mammals, type-A (CO_3^{2-} substituting OH^- groups) [11] and type-B carbonated apatite (CO_3^{2-} for PO_4^{3-} substitution). [9] The ratio of type-A to type-B carbonation in biological apatites is in between 0.7- 0.9. [12] Inclusion of carbonate ion into the structure of HAp results in decrease in crystallinity and increase in solubility of bone mineral both in vivo and in vitro. [13] Also biological apatites have relative crystallinity of 33-37%.[14, 15] The appearance of amorphous phase in HAp leads to increased tendency of resorption of the material. [16] Hence, it is reasonable to synthesize nonstoichiometric partly amorphous HAp with various substituted elements mimic to bone apatite to achieve improved bioactivity and osteoconductivity in comparison with pure and fully crystalline HAp ceramics.

Manganese is one of the important trace elements often present in small amounts (about 50 ppm) in the mineral phase of bones. [16] Mn^{2+} ions activate integrins, a family of receptors that mediates cellular interactions between extracellular matrix and cell surface ligands. [17] Presence of Mn^{2+} ions increase the ligand binding affinity of integrin and activate cell adhesion. [18] Mn-doped HAp favour osteoblasts proliferation, activation of their metabolism and differentiation. [19] Manganese helps in normal bone growth, bone metabolism and bone remodeling. Existence of Mn^{2+} ions in apatites helps in synthesis of mucopolysacharides, whereas deficiency of Mn content lowers the synthesis of organic matrix and retards endochondral osteogenesis causing bone abnormalities including decrease in thickness or length of bones and bone deformation. [20] Insufficience of Mn in bone probably causes osteoporosis. [21]

Previously Mn has been doped into HAp through the solid state reaction, [22] sol-gel, [23] wet chemical [16] and precipitation method. [24] But still there exist no reports on Mn insertion into HAp via mechanical alloying (MA). MA provides a fast and one step synthesis of different nanocrystalline powder materials. It has some unique advantages including simple synthesis technique, low fabrication cost and easy control over compositions. In addition to that it provides a fine homogeneous nanocrystalline powder that can be consolidated according to specific requirements. By this technique, productivity of nanocrystalline powders can be increased by controlling different parameters such as ball to powder mass ratio (BPMR), rotation speed, milling atmosphere, time of milling process, volume of the milling container etc.

In the present work, nanocrystalline Mn doped A-type carbonated HAp (A-cHAp) has been synthesized for the first time through mechanical alloying the $CaCO_3$ and $CaHPO_4.2H_2O$ and MnO powder precursors in open air medium. To understand the mechanisms of incorporation of Mn^{2+} as dopant in HAp, and to characterize multisubstituted (Mn and carbonate) nanocrystalline HAp, it is of great importance to carry out detailed structural characterization of substituted synthetic HAp. In this context microstructure characterization of nanocrystalline HAp samples in terms of different lattice imperfections along with quantitative estimation of different phases present in the as-milled samples were made by analyzing the X-ray powder diffraction (XRD) patterns employing Rietveld's structure refinement method. [25-30] It is well known that Rietveld's method is the best indirect approach for microstructural characterization of nanocrystalline materials containing a significant number of overlapping reflections. Therefore, the aims of the present work are to (i) synthesize nanocrystalline Mn doped HAp by MA, (ii) carry out microstructure characterization of nanocrystalline Mn doped HAp powder samples in terms of lattice imperfections by means of XRD and HRTEM, (iii) find out exact location of Mn insertion in the Mn doped HAp lattice structure and (iv) check cytocompatibility of the synthesized samples.

Materials and methods

Sample preparation and experimental

Synthesis of Mn doped A-type carbonated HAp (A-cHAp) through MA considering charge balance can be represented by the following equation:

$$(4\text{-}x)\ CaCO_3 + 6\ CaHPO_4.2H_2O + x\ MnO =$$

$$Ca_{10\text{-}x}Mn_x\ (PO_4)_6(OH)_{2\text{-}2y}\,(CO_3)_y + (4\text{-}x\text{-}y)\ CO_2 + (14\text{+}y)\ H_2O \qquad (1)$$

where $0 < x < 4$ and $0 < y < 1$

Mn doped A-cHAp nanocrystalline powders with three different compositions (x=0.25, 0.5 and 1.0) were synthesized with a (Ca+Mn)/P molar ratio 1.67 by dry milling the $CaCO_3$ (purity 99.5%, Merck), $CaHPO_4$. $2H_2O$ (purity 99%, Loba Chem.) and MnO (purity 99%, Sigma Aldrich) powder precursors taken in (4-x):6:x molar ratio for 10 h at room temperature in open air medium using a high energy planetary ball mill (P5, M/S Fritsch, GmbH, Germany). The undoped A-cHAP nanocrystalline powder was prepared by dry milling $CaCO_3$ and $CaHPO_4$. $2H_2O$ powders taken in 2:3 molar ratio for 10 h in air at room temperature. For both the undoped and doped samples the respective powder precursor mixtures placed in a hardened chrome-steel vial of 80 ml volume and then the sealed vial placed on the rotating disk of the ball mill and mechanical alloying of the mixture was carried out at room temperature in open air for 10 h with intermediate pauses of 10 min after each 20 min of milling.

XRD patterns of unmilled and all ball-milled powder mixtures were recorded with Ni-filtered CuK_α radiation (wavelength = 0.15418 nm) from an X-ray powder diffractometer (D8 Advance, Bruker) operated at 40 kV and 40 mA. For detailed X-ray whole profile analysis using Rietveld method, step-scan data (of step size $2\theta = 0.02°$ and counting time of 2s/step) were recorded in the 2θ range from 20° to 80°. Microstructure characterization of ball milled samples was also carried out by HRTEM operated at 200 kV (Model HR-TEM 2100F JEOL) and FESEM (JSM6700F, Jeol Ltd. Japan).

The FTIR spectra of as-milled undoped and Mn doped A-cHAp powders were obtained from the Perkin– Elmer FTIR spectrometer (Model RX1) in the transmission mode using KBr standard over a range of wavenumbers 400–4000 cm^{-1}.

Different valance states of Mn in the doped samples were determined by XPS spectroscopy using a spectrometer (Omicron Nano-Technology, Sl. No. 0571) with Mg K_{α} source (1253.6 eV), operated at 15mA emission current and 15 KV anode voltage.

Biological studies

Cell culture

HeLa cells were procured from NCCS, Pune and cultured in 10% FBS DMEM medium having 100 mg/L streptomycin and 100 IU/mL penicillin. Cell culture was done in a 25 mL cell culture flask and kept at 37°C in a humidified atmosphere of 5% CO_2 to about 70-80% confluence. In every 2-3 days, subculture was done and the media was changed after 48-72 h. The adherent cells were detached from the surface of the culture flask by trypsinization and subsequently used for used for cytotoxicity study. All the materials used in the cell culture study such as Dulbecco's Modified Eagles' Medium (DMEM), heat inactivated fetal bovine serum (FBS), trypsin from porcine pancreas, MTT [3-(4,5-dimethylthiazol-2-yl)-2,5-diphenyltetrazolium bromide], BSA-FITC were procured from Sigma Aldrich Chemical Company.

MTT assay

Cell viability of the Mn doped A-cHAp samples was assessed by the microculture MTT reduction assay as previously reported. [31] The assay involves the reduction of a soluble tetrazolium salt by mitochondrial dehydrogenase which was present only in viable cells to an insoluble colored formazan product. The colored product was dissolved in DMSO solvent. The amount of product formed was measured spectrophotometrically thereafter. The enzyme activity and the amount of the formazan produced were proportional to the number of alive cells. The mammalian HeLa cells were seeded at a density of 15,000 cells per well in a 96-well microtiter plate 18-24 h before the assay. A stock solution of the Mn-HAP sample in dispersed state was prepared in sterile water by sonication for 30 min. The concentration in the microtiter plate was varied from 5 to 100 µg/mL. The cells were incubated for 6, 12 and 24 h at 37°C under 5% CO_2 environment. The cells were further incubated for another 4 h in 15 µL MTT stock solution (5 mg/mL). The produced formazan was dissolved in DMSO and absorbance at 570 nm was measured using BioTek® Elisa Reader. The number of surviving cells were expressed as percent viability = (A_{570}(treated cells)-background)/ A_{570}(untreated cells)-background) × 100.

Method of analysis

The fundamental principles and theoretical aspects of the Rietveld's method of analysis of powder diffraction pattern are well described in the literatures. [25-28] In the present study, we have adopted the Rietveld's powder structure refinement method [25-30] for X-ray powder diffraction data analysis using MAUD software (version 2.26). [30] MAUD 2.26 is designed to refine simultaneously both structural (lattice parameters, atomic fractional coordinates, occupancies, thermal parameters, etc.) and microstructure parameters (particle size and r.m.s. lattice strain) through Marquardt least-squares method. As the peaks are appreciably broadened with asymmetry, all the diffraction profiles are fitted with a pseudo-Voigt function with asymmetry accounting for both the particle size and strain broadening of the experimental profiles. The background of each experimental pattern is fitted with a polynomial of degree five. The observed

X-ray powder diffraction patterns are initially simulated with the precursor materials, $CaCO_3$ (ICSD # 73446, rhombohedral, Sp. gr. R3c (H)), $CaHPO_4.2H_2O$ (ICSD # 98804, monoclinic, Sp. gr. Cc), $CaHPO_4$ (ICSD # 917, triclinic, Sp. gr. P-1), MnO (ICSD # 9864, cubic, Sp. gr. Fm-3m) and expected resultant phase, A-cHAp (ICSD # 171549, hexagonal, Sp. gr. $P6_3/m$) after MA. Initially, positions of all peaks are corrected by successive refinements of zero-shift error. The structural parameters, including lattice parameters, atomic coordinates, atomic occupancies etc and microstructure parameters such as particle size and r.m.s. lattice strain are obtained after proper fitting the experimental patterns with refined simulated patterns. Considering the integrated intensity of the peaks as a function of structural and microstructure parameters, the Marquardt least-squares procedure is adopted to reduce the difference between the observed and simulated patterns and this minimization was monitored by the reliability index parameter, R_{wp} (weighted residual error) and R_{exp} (expected error) defined, respectively, as

$$R_{wp} = \left[\frac{\sum_i w_i (I_0 - I_c)^2}{\sum_i w_i (I_0)^2} \right]^{1/2} \qquad (2)$$

$$R_{exp} = \left[\frac{(N - P)}{\sum_i w_i (I_0)^2} \right]^{1/2} \qquad (3)$$

where I_0 and I_C are the experimental and calculated intensities, w_i (=1/I_0) and N are the weight and number of experimental observations and P the number of fitting parameters. This leads to the value of goodness of fit (GoF) defined as, GoF =R_{wp}/R_{exp}. [25-30]

The peak broadening, peak asymmetry and peak shift of the experimental profiles are fitted by refining the particle size, lattice strain and lattice parameter values (including zero-shift error). Refinements of all parameters are carried out until convergence is obtained with the value of

GoF very close to 1.0 (varies between 1.2 and 1.35 for the present case) confirming the goodness of refinement. The Caglioti parameters U, V, and W, [29] instrumental asymmetry and Gaussianity parameters [30] are obtained for the instrumental setup using a specially prepared Si standard and kept fixed during refinements.

Results and discussions

Phase confirmation from XRD

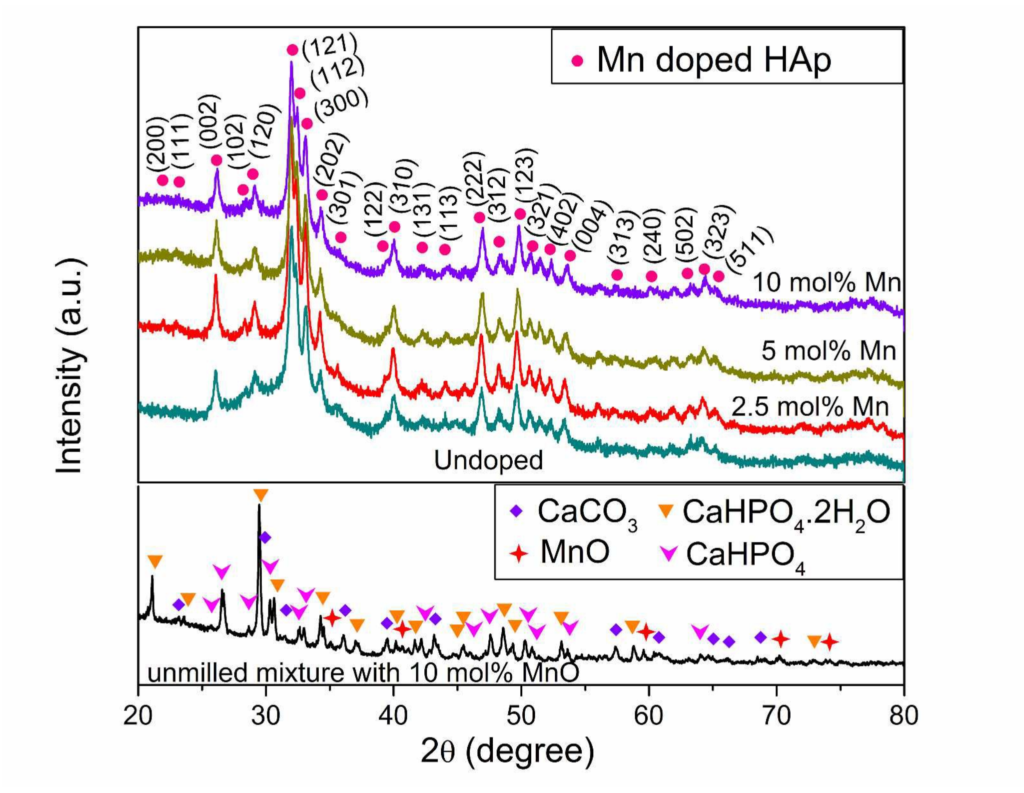

Fig. 1 XRD patterns of $CaCO_3$, $CaHPO_4.2H_2O$ and MnO powder unmilled mixture and milled for 10h with different mol% of Mn.

The XRD patterns of nanocrystalline undoped and Mn doped HAp powder synthesized by mechanical alloying the $CaCO_3$ and $CaHPO_4.2H_2O$ powder mixture taken in 2:3 molar ratio and $CaCO_3$, $CaHPO_4.2H_2O$ and MnO taken in (4-x):6:x molar ratio (x values 0.25, 0.5and 1.0) respectively are shown in Fig. 1. In the unmilled powder mixture the reflections of $CaCO_3$ (ICSD # 73446, rhombohedral, Sp. gr. R3c (H), a=4.991Å c=17.062Å), $CaHPO_4.2H_2O$ (ICSD # 98804, monoclinic, Sp. gr. Cc, a= 6.41Å, b= 15.18Å, c= 5.86Å, β= 119.20°), $CaHPO_4$ (ICSD # 917, triclinic, Sp. gr. P-1, a= 6.91Å, b= 6.62Å, c= 6.99Å,α=96.34°, β= 103.82°, γ=88.33°) and MnO (ICSD # 9864, cubic, Sp. gr. Fm-3m, a=4.446Å) reflections are present. However, we have found the presence of triclinic $CaHPO_4$ in the unmilled mixture though it was not present as the initial precursor. It is clearly evident from the figure that the XRD pattern of unmilled sample contains very sharp reflections indicating that the ingredients in the unmilled powder mixture have quite large particle sizes and they are almost free from any lattice strain. This indicates the initial precursors are well crystalline in nature. After 10 h of milling, all the precursor phase reflections are completely absent in the XRD pattern and the single HAp phase has been synthesized by mechanical alloying the powder mixtures for 10 h in open air. It is to be noted that this HAp powder is free from any contamination, either from precursors or from the milling media.

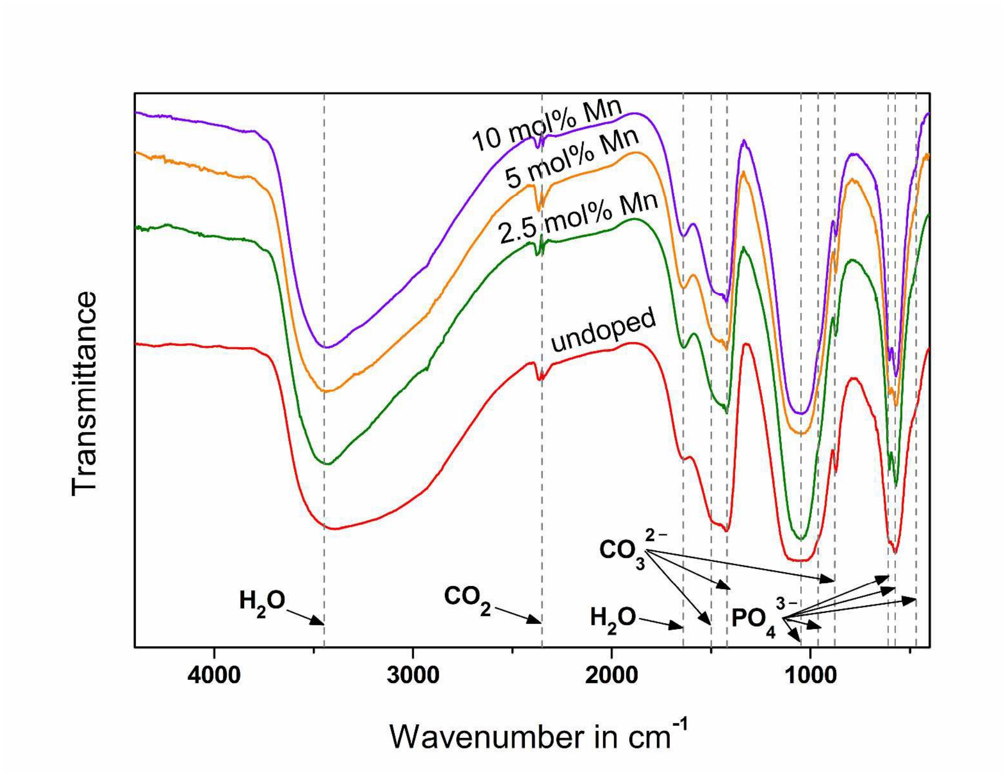

Fig. 2 FTIR spectra of as-milled undoped and Mn doped samples with different mol % of Mn content.

Confirmation of carbonation in HAp by FTIR analysis

FTIR spectra of as-milled HAp powders are shown in Fig. 2. The FTIR spectra reveal significant amounts of structural carbonate in all as-milled apatite samples. Two regions of the spectra are characteristic of carbonate vibrations in the as-milled samples (Fig. 2) [32] :

(1) 850–890 cm^{-1} assigned to ν_2 vibrations of carbonate groups

(2) 1400–1600 cm^{-1} assigned to ν_3 vibrations of carbonate groups.

In the first region the sharp band at 878 cm^{-1} in the FTIR spectra corresponds to ν_2 bending vibration of C-O bonds in carbonate group which is the characteristic of A-type carbonation in

HAp (substitution of CO_3^{2-} for OH^- channel ions). [33,34] In the another region there appears a relatively broad band within 1400-1580 cm^{-1} due to ν_3 stretching vibration of CO_3^{2-} group in all the as-milled samples. [35-37] This broad band comprises of three overlapping frequencies of ν_3, 1470 cm^{-1} and 1550 cm^{-1} due to A-type and 1419 cm^{-1} due to B-type carbonation (substitution of CO_3^{2-} for PO_4^{3-} ions). [38, 39] Therefore, both types of carbonation (A-type and B-type) are present in the samples. However, in the entire spectra we did not notice any prominent bands resulting from vibration of OH^- group which are usually present at 630 (libration mode) and 3570 cm^{-1}(stretching vibration). [32-42] It confirms the complete A-type substitution of CO_3^{2-} for OH^-. Whereas, all bands resulting from PO_4^{3-} vibrations are significantly prominent. So it is clear that the content of A-type carbonation is very high compared to that of B-type one. Thus, the dominance of A-type carbonation over B-type carbonation inspired us to designate the synthesized samples as A-cHAp.

FTIR spectrum of all the as-milled samples shows characteristic bands due to PO_4^{3-} ions. Among the phosphate derived bands the vibration band at 472 cm^{-1} in the spectrum corresponds to phosphate asymmetric stretching (ν_2) vibration. The doublets at 561 & 598 cm^{-1} are assigned to phosphate bending mode (ν_4) vibration. The band at 957 cm^{-1} results from symmetric stretching (ν_1) vibration of P-O bonds whereas the band between 1038 cm^{-1} and 1106 cm^{-1} is due to P-O asymmetric stretching (ν_3) vibration. [40-42]

The broad band at 3400 cm^{-1} and another band at 1640 cm^{-1} are attributed to the presence of water adsorbed by the HAp molecule. [43] The absorption band present at 2350 cm^{-1} in all the samples corresponds to CO_2 absorption by the sample.

Structural and microstructure characterization by Rietveld's method

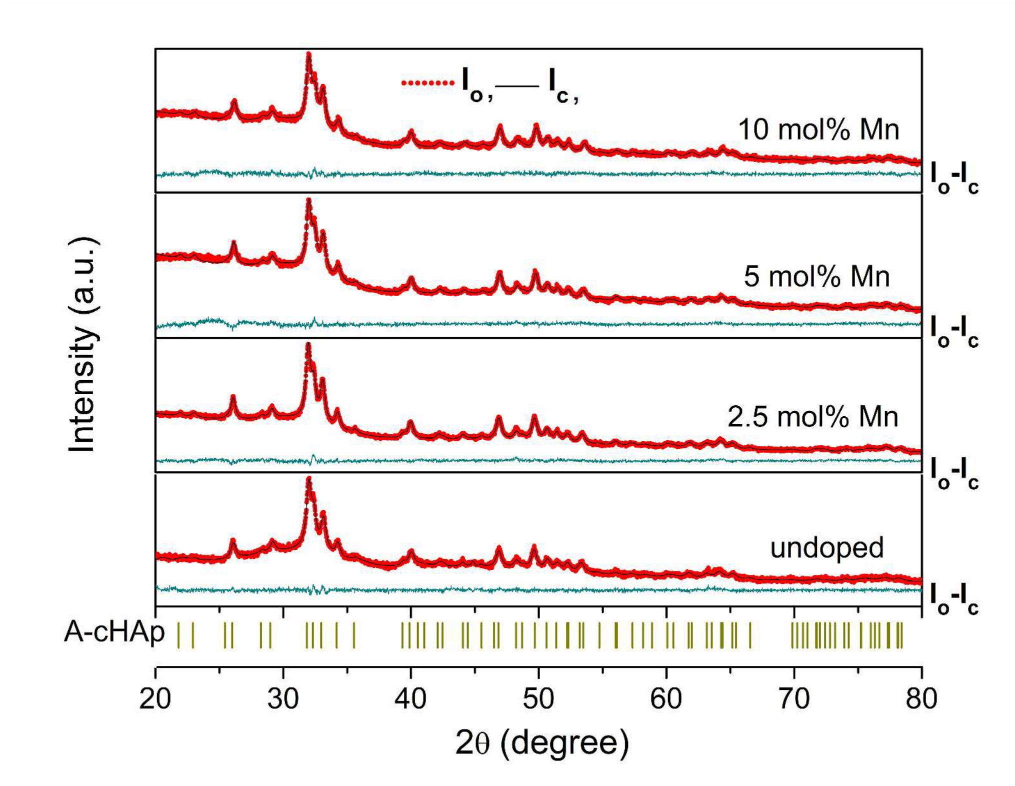

Fig. 3 Rietveld analysis output of the XRD pattern of as-milled undoped and Mn doped A-cHAp samples with different mol % of Mn content.

Experimental XRD patterns of all as-milled samples are fitted by refining the structural and microstructure parameters of respective simulated patterns with 'goodness of fittings' (GoFs) lying between 1.2 and 1.35; suggesting the good fitting qualities for all the experimental patterns. The fitted XRD patterns of the samples are shown in Fig. 3. The residual of fittings (I_O−I_C) between observed (I_O) and calculated (I_C) intensities of each fitting is plotted under respective XRD patterns. The Rietveld's analysis of all the XRD patterns confirms the complete formation of single phase A-cHAp and up to 10 mol % full incorporation of Mn into A-cHAp is obtained by MA. Peak positions of A-cHAp reflections are marked (|) at the bottom of the plot in

Fig. 3. The observed peak broadening of Mn doped A-cHAp solid solution in the course of milling may be attributed to the effect of both small particle size and lattice strain developed inside the lattice due to constant fracture and rewelding mechanism of MA and substitution of Ca^{2+} ions (ionic radius = 0.99 Ǻ) by relatively smaller Mn^{2+} ions (ionic radius = 0.83 Ǻ).

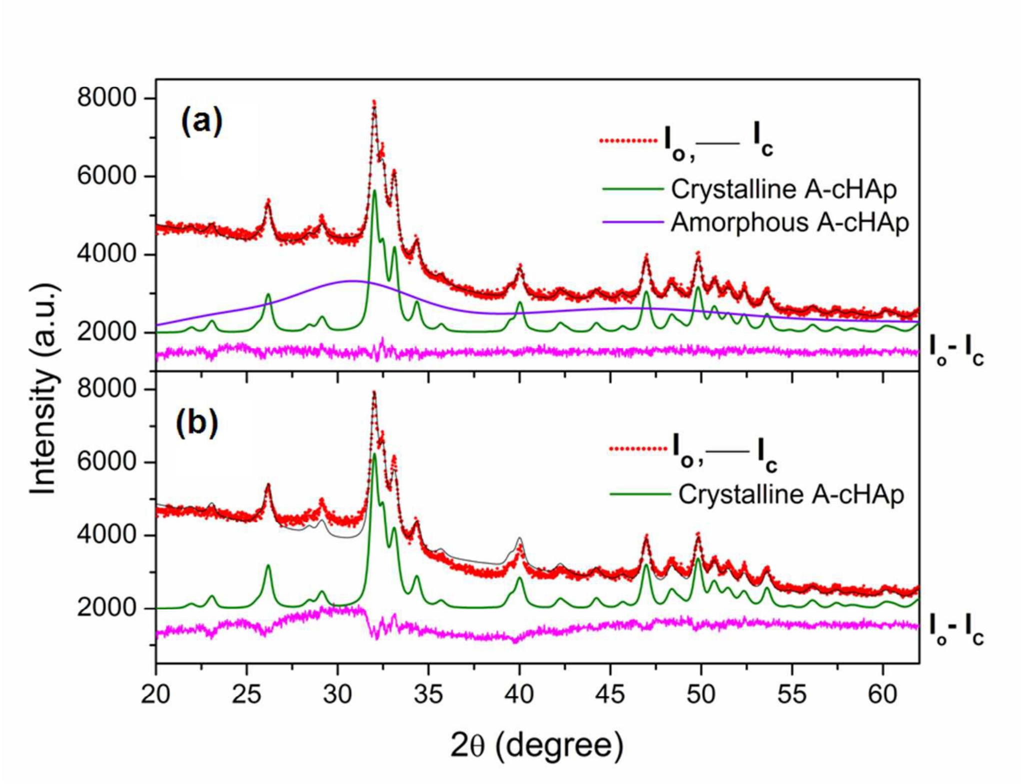

Fig. 4 Rietveld output plot of 10 mol% Mn doped A-cHAp fitted with (a) both crystalline and amorphous A-cHAp phases and (b) with only crystalline A-cHAp phase.

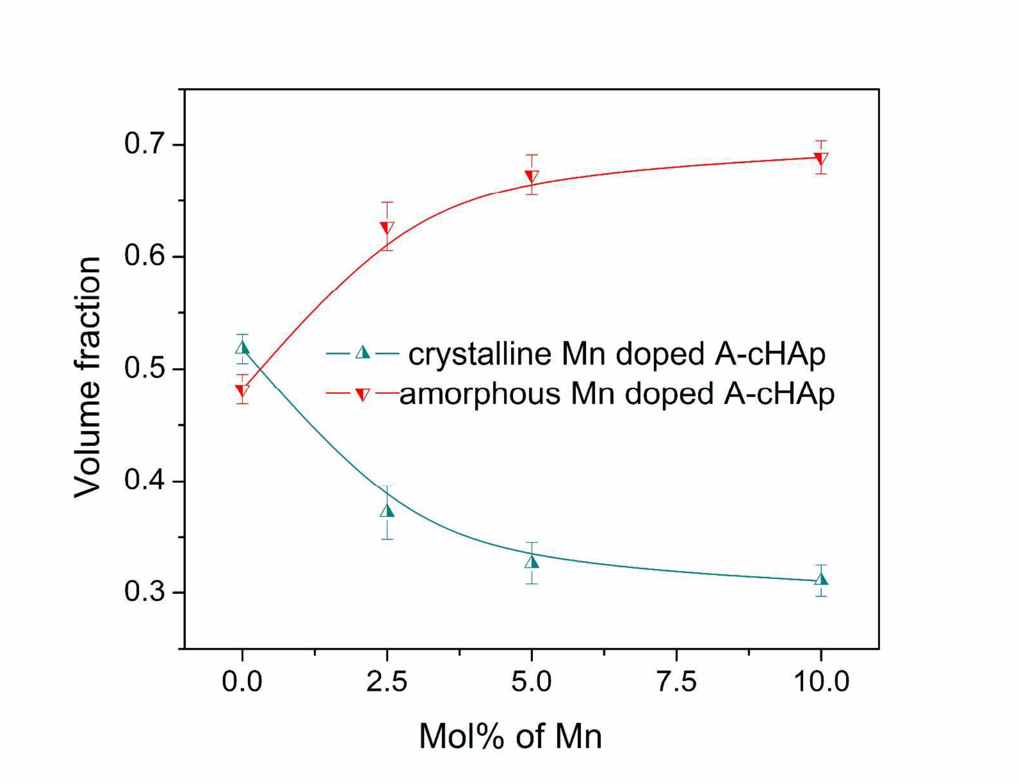

Fig. 5 Variation of volume fractions of different phases present in the as-milled samples with different mol% of Mn doping.

From Rietveld's analysis it is found that a part of crystalline HAp has been transformed to amorphous phase due to cumulative effect of Mn incorporation into HAp lattice and continuous high energy impact of MA for 10h of duration. We have fitted the XRD patterns of all the as-milled samples without and with an additional amorphous A-cHAp phase with very low particle size and high strain along with crystalline A-cHAp phase and such a plot for 10 mol% Mn doped sample is shown in Fig. 4. It can be noted that when the XRD pattern fitted only with crystalline phase (Fig. 4(b)) the quality of fitting was very poor and the un-matched intensity pattern at around 30° and 38° 2θ indicates the presence of an amorphous like phase, similar to distorted to crystalline A-cHAp phase. Inclusion of the amorphous phase results in perfect fitting of the XRD pattern (Fig. 4(a)) and the Rietveld refinement reveals the measure of different microstructure parameters along with the quantitative estimation of crystalline and amorphous phases. The relative phase abundance of crystalline and amorphous A-cHAp as obtained from Rietveld's analysis is shown in Fig. 5. In undoped A-cHAp almost 50% amorphization is obtained due to MA and in addition to this inclusion of Mn^{2+} ions into HAp structure leads to increase this amorphization up to ~ 70% for 10 mol% Mn doped A-cHAp. From the perspective of amorphous content in native biological apatites (~ 63%-67%) [14, 15] the prepared HAp can be considered as excellent biomimetic product for bone transplantation. Such amorphization should also improve the mechanical properties of HAp along with homogeneous bone resorption [16].

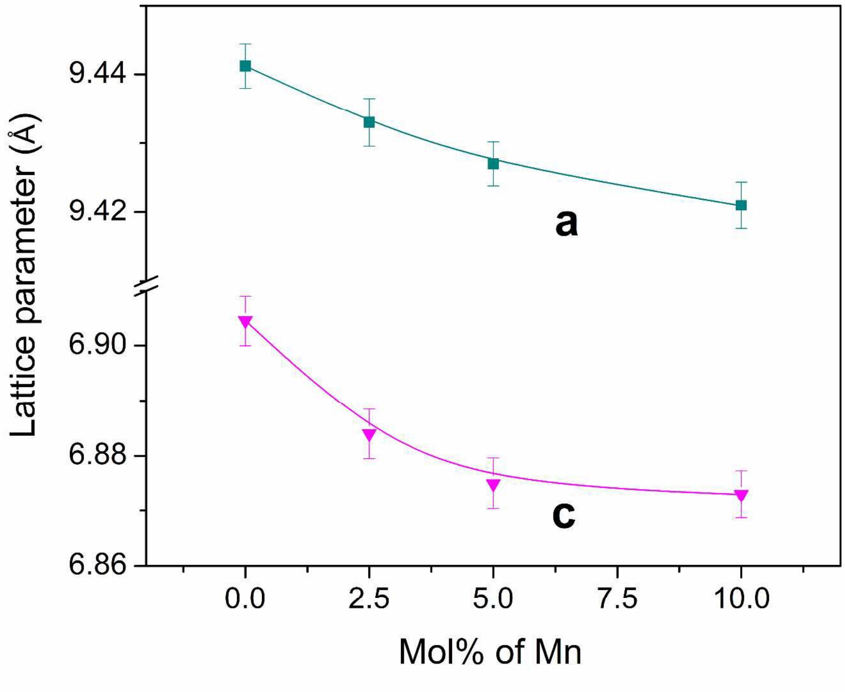

Fig. 6 Variation of lattice parameters of hexagonal Mn doped A-cHAp phase with different mol % of Mn content.

Variation of lattice parameters a and c of hexagonal A-cHAp phase with increasing doping percentage of Mn in all compositions are shown in Fig. 6. The lattice parameter a decreases slowly whereas lattice parameter c decreases relatively at a faster rate with increasing doping concentration of Mn. Such decrease in lattice parameters can be endorsed to the continuous substitution of Ca^{2+} ions by the smaller Mn^{2+} ions during solid solution formation.

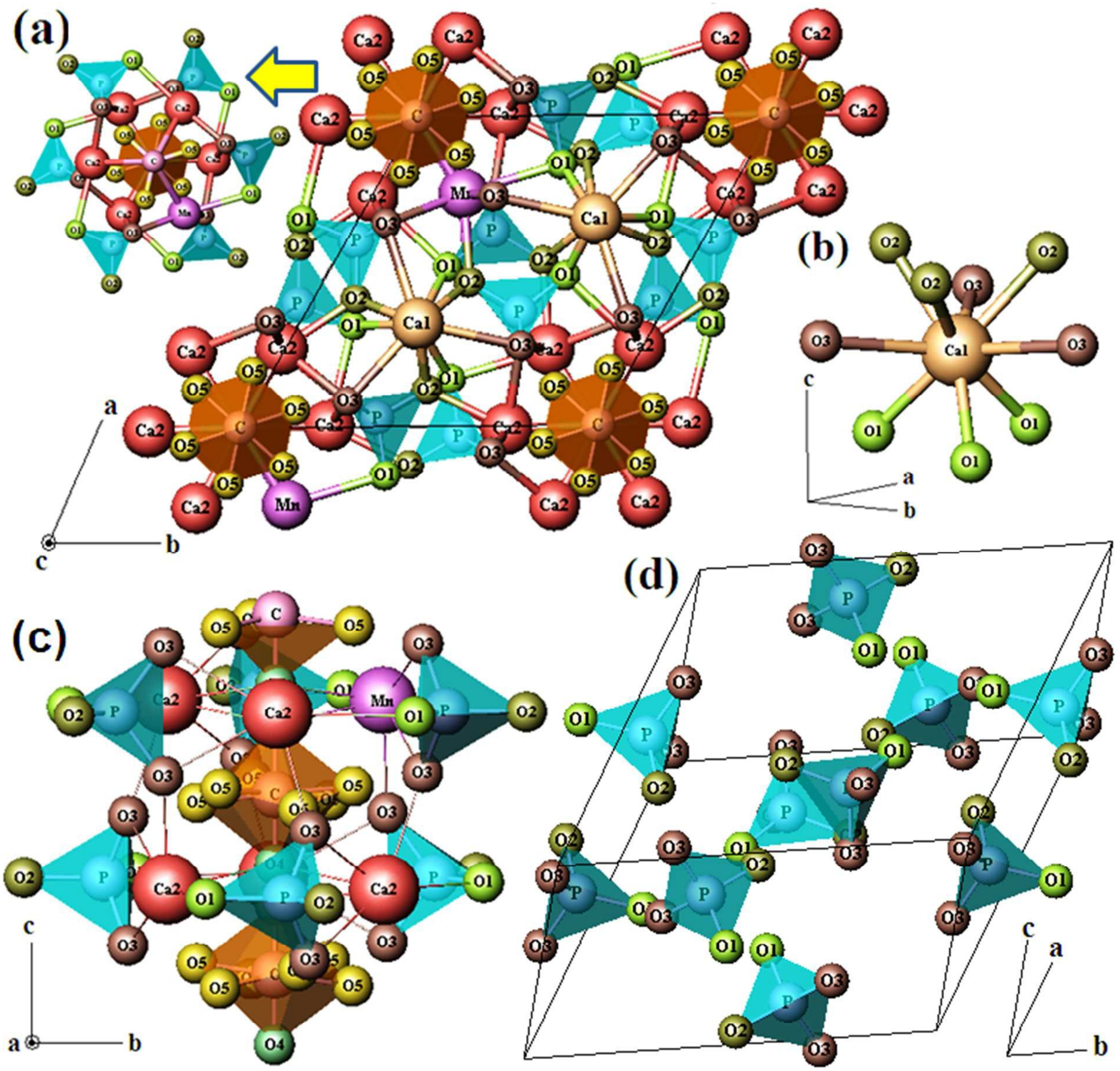

Fig. 7 (a) Representation of the Mn-substituted A-cHAp structure: general view along **c**-axis. Inset of the Fig: Carbonate hexagonal channel, looking along the **c**-axis, (b) Structure of $Ca1O_9$ polyhedron. (c) Local environment of carbonate hexagonal channel, looking along the **a**-axis. (d) Distribution of PO_4 tetrahedrons in and around A-cHAp unit cell.

There are two nonequivalent Ca sites; Ca1 and Ca2, in A-cHAp which are replaced by the substitutional cations. Local atomic arrangements of Ca1 and Ca2 are illustrated in Fig. 7(a). The Ca1 site is surrounded by six PO_4^{3-} tetrahedral, where six oxygen ions (designated as O1 and O2) at the vertices of PO_4^{3-} tetrahedral are located at the first nearest neighboring sites and other three oxygen ions (designated as O3) are present at the second nearest neighboring sites, forming the $Ca1O_9$ substructure as shown in Fig. 7(b). Whereas six $Ca2^{2+}$ ions surrounding the C-O channel of A-cHAp lattice forms hexagonal channel along the **c**-direction as shown in the inset of Fig. 7(a). Among these six $Ca2^{2+}$ ions, one group consisting of three Ca2 forms a triangle located at 1/4 **c** and the other group of three forms another triangle at 3/4 **c** of the structure (Fig. 7(c)). In the C-O channel of A-cHAp lattice, each C atom (fractional coordinate (0,0,0)) is surrounded by six O5 atoms forming hexagonal channel along **c**. In Fig. 7(d) the arrangement of PO_4 polyhedrons in and around A-cHAp unit cell is shown. Out of these ten polyhedrons, two lie at the centre of the unit cell and the rest eight remain at the **ac** or **bc** face of the unit cell [Fig. 7(a) and (d)].

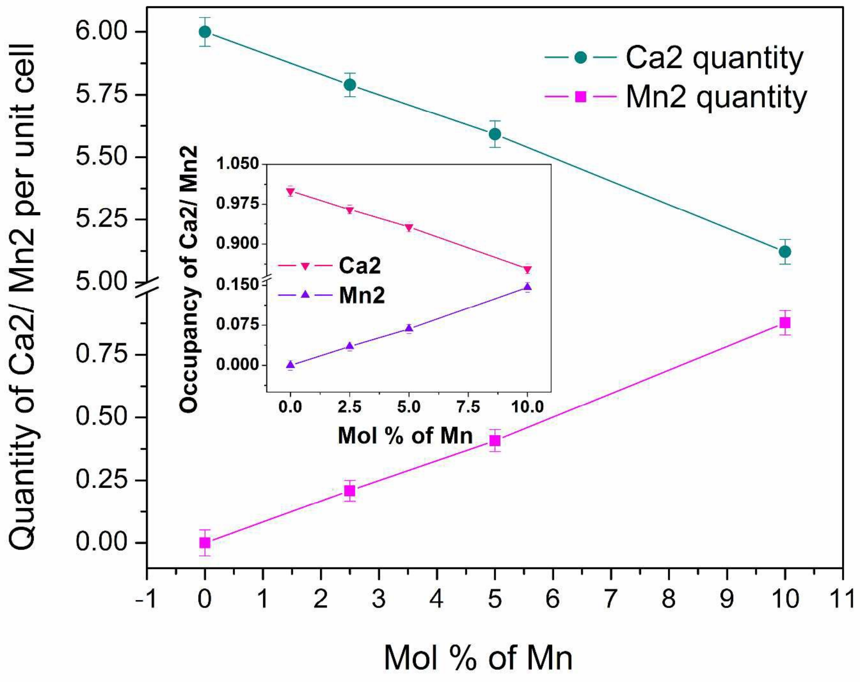

Fig. 8 Variation of quantity of Ca2/ Mn2 atoms per unit cell in all as-milled samples with increasing Mn content. Inset of the Fig. shows the variation of occupancy of Ca2/ Mn2 atoms in all as-milled samples.

Significant amount of research works were carried out on the Mn-substituted apatites in order to explain the exact structural role of Mn in bone. Mn^{2+} ions were reported to replace Ca^{2+} ions in HAp lattice. [18-20, 23, 24, 44] However, the exact location of Mn in the substituted HAp unit cell is still ambiguous: does it replace Ca1 (columnar Ca atoms parallel to c axis) or Ca2 (triangular Ca site about the C-O channel along the **c** axis of A-cHAp), resulting different local environments in the lattice? In only one existing ESR spectroscopy study, Pon-On et al. [44] reported that the Mn^{2+} ions substituted the ninefold coordinated $Ca1^{2+}$ ions. In the present study, to find out the exact location of Mn substitution in the A-cHAp unit cell, occupancies of both

Ca1 and Ca2 sites in the A-cHAp structure were refined carefully considering the possibilities of substitution of these sites by Mn1 and Mn2 atoms respectively. After thorough refinement the occupancy of Ca2 site found to reduce by a significant amount whereas that of Ca1 site remained almost invariant. Consequently, the occupancy of Mn2 site took a significant value. The variation of site occupancies of Ca2 and Mn2 atoms per unit cell with increasing Mn concentration are shown in Fig. 8. It is evident from the figure that the number of Ca2 atoms in undoped A-cHAp unit cell is 6 and it decreases continuously to nearly 5 with increase in Mn substitution into A-cHAp from 0.00 to almost 1.00. The occupancy of Ca2 decreases accordingly with decrease in quantity of Ca2. Therefore, Rietveld's analysis confirms the substitution of Ca2 atoms with Mn atoms, contrary to the findings of Pon-On et al., [44] may be due to different synthesis process. However, Ca2 site is expected to be energetically more favorable than Ca1 site for Mn substitution. [45-47]

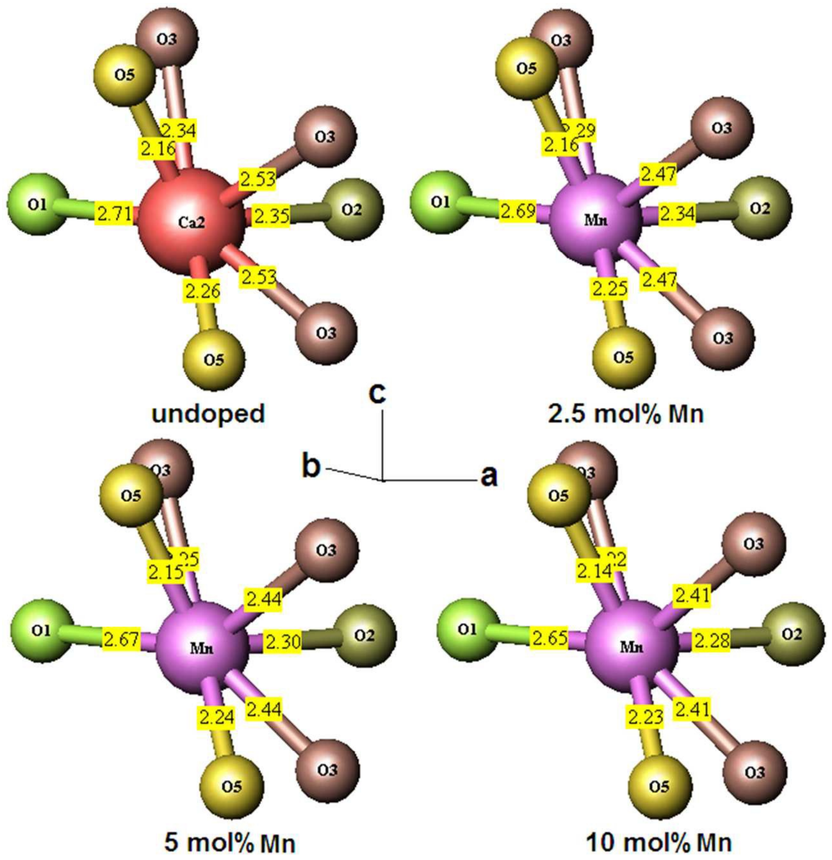

Fig. 9 Changes in Ca2/Mn – O bond lengths (Å) in different Mn doped samples in comparison to undoped sample.

Substitution of Ca2 site by Mn is manifested in significant changes in bond lengths between Ca2/Mn and O sites in undoped and Mn-doped A-cHAp with different percentage of Mn content and these changes have been depicted in Fig. 9. It is evident that in undoped sample Ca2–O bonds are of different lengths, similar to John-Teller distortions in A-cHAp lattice. In Mn doped samples all Ca2/Mn–O bond lengths decrease, in general with different rates, from the undoped one and these contractions increased further with increase in Mn mol%. It may be noted that in undoped HAp one of the Ca2 – O3 bond with 2.34Å bond length is almost parallel to **c**-axis and the other two Ca2 – O3 bonds with 2.53Å bond lengths make ~45° bond angle with **c**-

axis. The Ca2-O1 and Ca2-O2 bond lengths are also unequal and parallel to **b-** and **a** -axis respectively. After Mn doping, maximum contraction is noticed for Ca2 – O3 bonds in comparison to both Ca2/Mn–O1 and Ca2/Mn–O2 bond lengths and the degree of contraction increases with increasing Mn concentrations. This may be due to the fact that the decrease in lattice parameter c is more than a in doped samples. It is also noticed that the Ca2-O1: Ca2-O2 bond length ratio 1.153 in undoped sample increases gradually to 1.162 and Ca2-O3 (making 45° with **c** axis): Ca2-O3 (parallel to **c**) ratio also increases from 1.081 to 1.086 with increase in Mn doping concentrations to 10 mol%. It indicates that the lattice distortion increases with increasing doping concentrations. It may lead to increase disorderness in the lattice and results in transformation of crystalline to amorphous like HAp phase. However, the change in Ca2/Mn – O5 bonds is small as O5 sites are connected to C atoms residing at 2b Wyckoff position with fixed (0,0,0) coordinate and did not respond to lattice distortion significantly. It appears that the O5 site approaches slowly to Ca2/Mn atom during substitution of $Ca2^{2+}$ position by smaller Mn^{2+}. Therefore the overall results confirm the substitution of Mn^{2+} in $Ca2^{2+}$ site only.

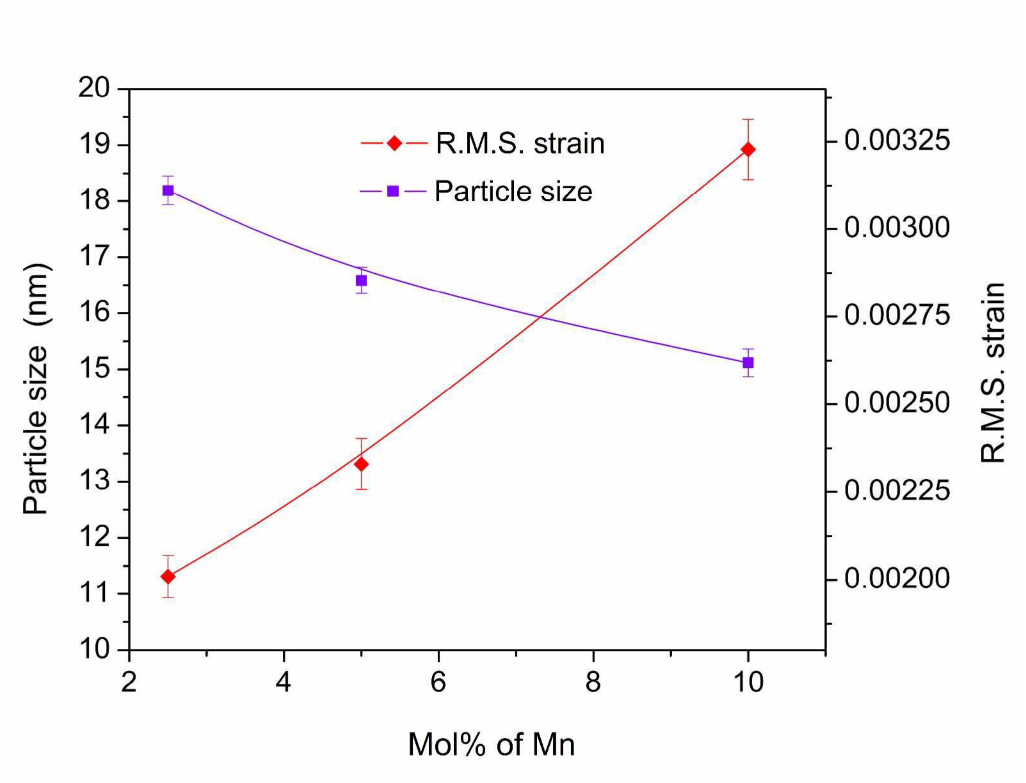

Fig. 10 Variations in crystallite size and r.m.s. strain of Mn doped A-cHAp with increasing Mn doping.

The Rietveld analysis is a superior technique to explore the shape and size of crystallite in a powder sample. It reveals that crystallites of all doped samples are isotropic in nature. Variations of crystallite size with different mol% of Mn doping obtained from Rietveld analysis are shown in Fig. 10. The crystallite size of 2.5 mol% doped sample is found to be ~ 18 nm which reduces slowly to ~ 15 nm for 10 mol% Mn doping. The r.m.s. lattice strain generated in doped A-cHAp lattice during the milling as well as Mn substitution has also been obtained from the Rietveld analysis and shown in Fig. 10. As crystallite size decreases, r.m.s lattice strain generated within the lattice gradually increases. Consequently, we notice that the r.m.s lattice strain significantly increases with increasing Mn doping. These results signify the dominance of strain broadening over particle size broadening in the XRD patterns.

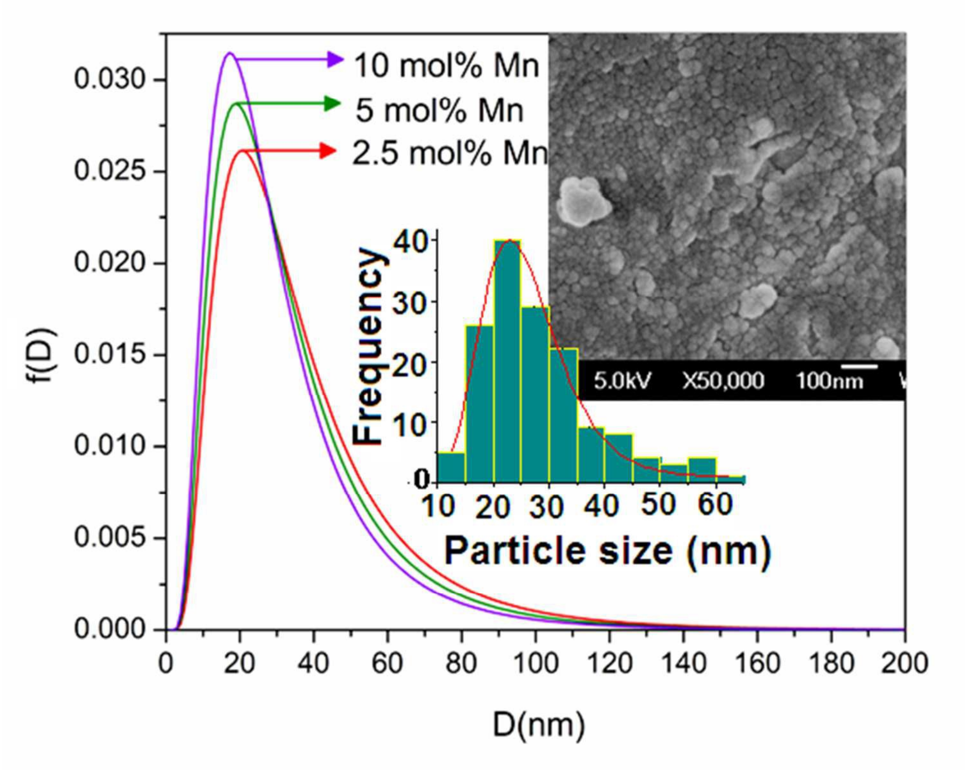

Fig. 11 Distribution of crystallite sizes of Mn doped A-cHAP samples with different Mn content. Inset of the Fig.: FESEM image of 10 mol% Mn doped A-cHAp particles and distribution of particle size as-revealed from the image analysis.

Fig. 11 depicts the variation of crystallite size distributions for different mol% of Mn doping. We see that with increasing Mn content the size distribution becomes slightly narrower. The most probable values in the respective distribution curves are very close to those shown in Fig. 10. Similar kind of distribution of spherical particles (area weighted) has also been obtained from FESEM image and shown in the inset of Fig. 11, in which the most probable particle size value is very close to the crystallite size obtained from the Rietveld analysis.

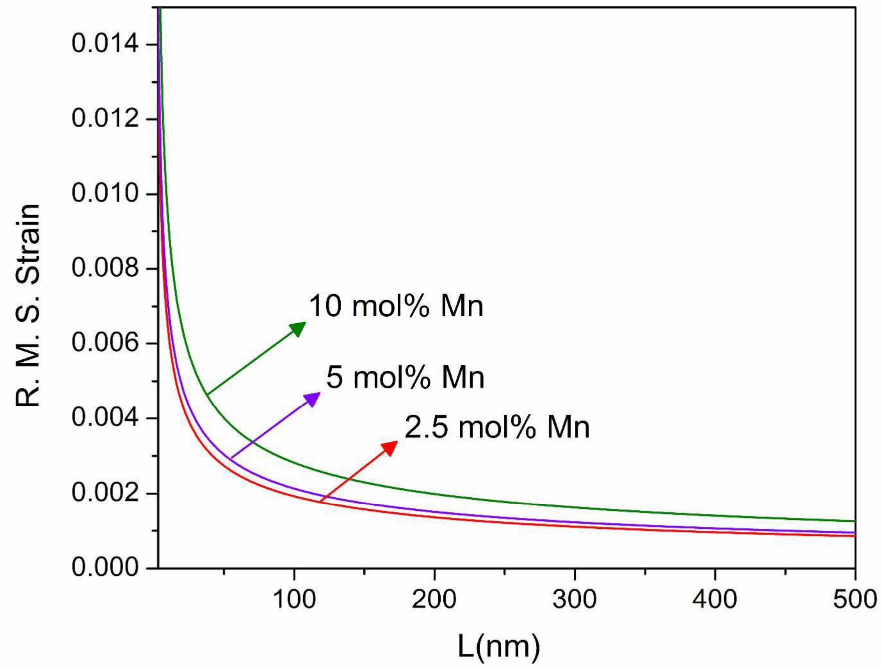

Fig. 12 Distributions of r.m.s. strain of Mn doped A-cHAp samples at different percentage of Mn doping. (L=na$_3$, n =harmonic number, a$_3$=lattice parameter).

The distributions of lattice strain inside the particle are shown in Fig. 12. From the nature of variation of strain distributions it is obvious that the lattice strain increases significantly for higher percentage of Mn substitution. It is evident from the plot that the lattice strains generated in A-cHAp during ball milling are extended over a long period L ~500 nm (L= na$_3$, n is integer and a$_3$ is the lattice parameter) and increase significantly in relatively higher mol% of Mn doping. It may also be noted that the lattice strains are extended to a longer period with increasing Mn content due to mismatch in atomic radii between Ca^{2+} and Mn^{2+}.

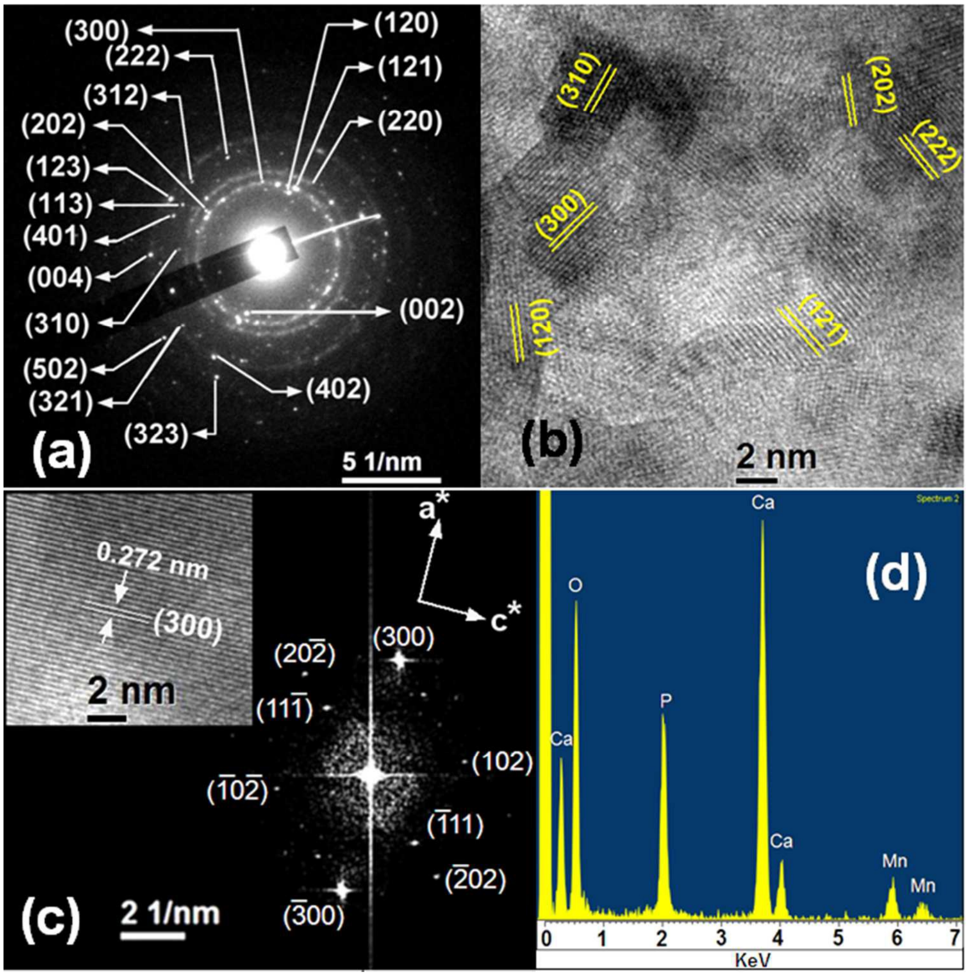

Fig. 13 (a) Selected area electron diffraction (SAED) pattern of 10h milled 10 mol% Mn doped A-cHAp powder, (b) HRTEM micrograph of different planes with different d-values, (c) The FFT pattern of the region shown in the inset, (d) EDX spectrum of 10 mol% Mn doped A-cHAp.

HRTEM analysis

The HRTEM micrographs of the A-cHAp sample synthesized with 10 mol% Mn content shown in Fig. 13. The selected area electron diffraction (SAED) pattern of 10 h milled sample confirms the formation of nanocrystalline hexagonal HAp phase (Fig. 13(a)). Simultaneous presence of different spots and rings in the SAED pattern is due to distribution in particle sizes.

These reflections are indexed properly as per the ICSD # 171549 (Sp. gr. $P6_3/m$) and the intensity distributions of each individual reflection are in accordance with the XRD patterns of the milled sample shown in Fig.1. A selected portion of HAp powdered sample is magnified in HRTEM image (Fig. 13(b)) which reveals almost random orientation of some of the HAp nanoparticles. Measure of interplanar spacings (d_{hkl}) confirms the presence (120), (121), (202), (300), (310) and (222) lattice planes of HAp lattice as shown in Fig. 13(a). The perfectly parallel lattice fringes predict that the particles are free from lattice imperfections. The FFT pattern of the region shown in the inset of Fig. 13(c) taken along **b** crystallographic axis is shown in Fig. 13(c). The most intense spot in the FFT pattern corresponds to (300) reflection consistent with the inset lattice fringe pattern. Presence of the halo around the centre of the pattern can be assigned to the existence of amorphous phase in the sample. Some other diffraction spots in the FFT pattern are identified and indexed with the A-cHAp lattice. From the EDX spectrum shown in Fig. 13(d), it is found that Ca/P molar ratio for 10 mol% Mn doped sample decreased from the value 1.67 (pure HAp) to 1.54. While the (Mn+Ca)/P molar ratio becomes 1.68, indicating that Ca^{2+} ions in the lattice are replaced by the Mn^{2+} ions. However, Ca/Mn molar ratio is found to be 11.28 which is slightly greater than the theoretical value of 10 mol% doping. This inconsistency may be due to very localized exposure of the electron beam on the sample for composition analysis of Mn doped sample.

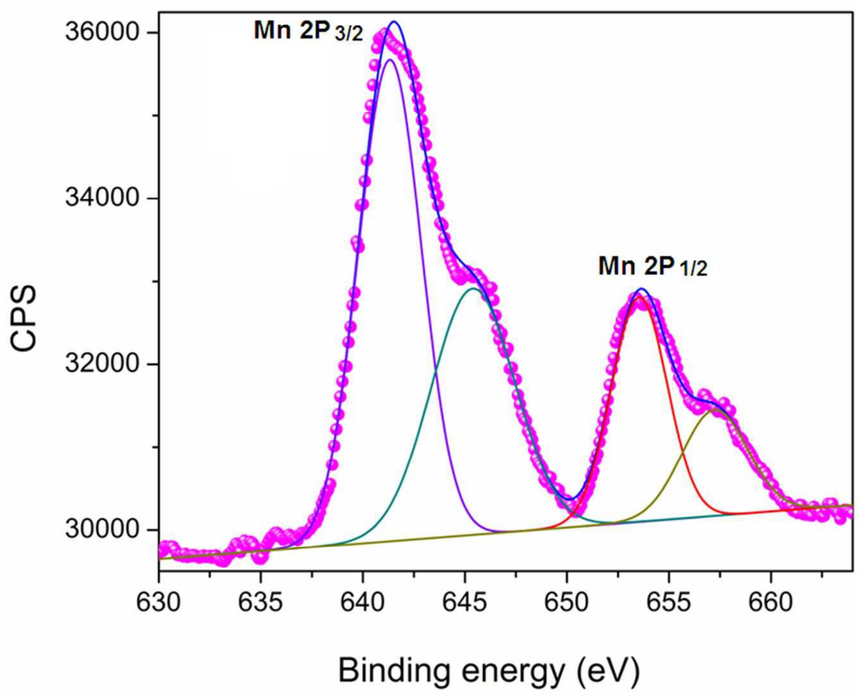

Fig. 14 Mn 2p XPS spectra of 10 mol% Mn doped A-cHAp powder.

XPS analysis

XPS spectroscopy has been used to determine the valance state of Mn in the doped samples. Fig. 14 represents the typical Mn 2p XPS spectra of 10 mol% Mn doped A-cHAp powder. The strongest peak is present at 641.3 eV and an additional peak at 653.6 eV belonging to $2p_{3/2}$ and $2p_{1/2}$ levels of Mn respectively. Both the peaks have a satellite ("shake-up") feature at 645.4 eV and 656.9 eV. The main $2p_{3/2}$ peak can be assigned to the positions of MnO at 640.3 – 641.4 eV or Mn_2O_3 at 641.5– 641.7 eV correspond to Mn^{2+} or Mn^{3+} valance states respectively. [48] However, MnO has a satellite feature (~ 645 eV) for $2p_{3/2}$ and (~ 657 eV) for $2p_{1/2}$ which is not present for either Mn_2O_3 or MnO_2 [49, 50] confirming the presence of Mn^{2+} ions in the synthesized samples. As the difference of binding energy of different Mn ions are very small therefore low concentration of Mn^{3+} can be excluded and presence of divalent Mn ions should be dominating.

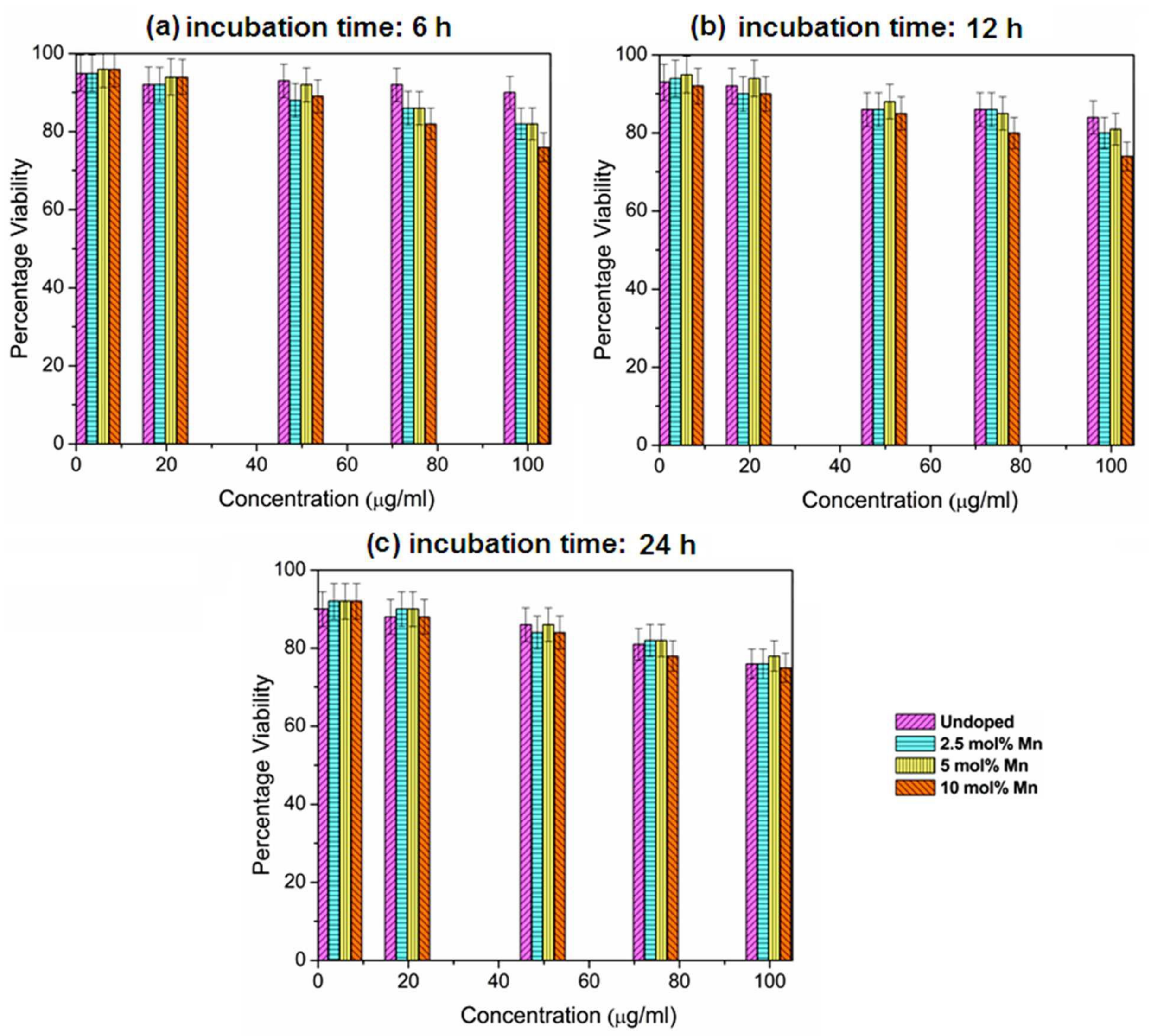

Fig. 15 Viability of HeLa cells treated with varying concentrations of Mn doped A-cHAp incubated for (a) 6 h, (b) 12 h and (c) 24 h. Percent errors are within ±5% in triplicate experiments.

Cytocompatibility test

The cytocompatibility of the Mn doped A-cHAp samples is analyzed using colorimetric MTT assay. Initially, stock solutions of the samples are prepared having a concentration of 1000 μg/mL. Each sample is prepared by sonication for 30 min and instantaneously adding the samples to the cells. Samples are incubated with mammalian human cell line (HeLa cells) separately for 6, 12 and 24 h. More than 85% or equal to 85% cells are alive in undoped and all three samples with 2.5, 5 and 10 mol% of Mn doping up to 50 μg/mL and with further increase in the concentration, percentage viability of the cells marginally decreased to around 80% upto a concentration of 100 μg/mL for all incubation time intervals 6, 12 and 24 h (Fig. 15(a), (b) and (c) respectively). Thus, it can be concluded that all the four samples showed sufficiently high percentage cell viability (~85%) after 24 h of incubation upto 50 μg/mL concentration and (~80%) upto 100 μg/mL.

Conclusions

Nanocrystalline single phase Mn doped A-type carbonated HAp powder is synthesized at room temperature by mechanical alloying the $CaCO_3$, $CaHPO_4.2H_2O$ and MnO powder mixture. FTIR spectra analysis reveals A-type carbonation (substitution of CO_3^{2-} for OH^-) in HAp lattice. Hence, mechanical alloying (MA) has been proved to be a novel method for the synthesis of carbonated HAp. To the best of our knowledge, this is the first time report on doping of Mn into HAp by mechanical alloying. Rietveld refinement of XRD patterns reveals detailed microstructure characterization in terms of lattice imperfections, measures the relative abundance of crystalline and amorphous and confirms the substitution of $Ca2^{2+}$ by Mn^{2+} in Mn doped A-cHAp lattice. HRTEM image analyses confirm the presence of an amorphous phase originated due to cumulative effect of mechanical alloying and Mn substitution in HAp lattice. The content of amorphous HAp phase in the synthesized samples is similar to that found in biological apatite present in bone. Overall structural analysis reveals that the synthesized HAp samples are very close in composition and the structure of HAp is analogous to native bone apatite. It can therefore be used as an excellent biomimetic product for bone transplantation. Mn^{2+} valance state in A-cHAp lattice is confirmed by XPS spectra analysis. MTT assay reveals high percentage of cell viability and hence confirms the cytocompatibility of the Mn doped A-cHAp samples.

Acknowledgement

Authors (SKP and SL) wish to thank UGC-DAE consortium for Scientific Research, Kolkata centre for providing the XRD facility and Mr. P.V. Rajesh for recording the XRD data. The University Grants Commission (UGC), India is acknowledged for granting CAS-I programme under the thrust area “Condensed Matter Physics including Laser Applications” to the Dept. of Physics, The University of Burdwan under the financial assistance of which this work has been carried out. Authors also acknowledge Prof. B.K. Ghosh of Dept. of Chemistry, The University of Burdwan for providing the FTIR facility.

References

[1] J. C. Elliott, *Structure and chemistry of the apatites and other calcium orthophosphates*, Elsevier, Amsterdam, 2nd edn., 1994, vol. **18**, ch. 3. pp. 111-189.

[2] M. J. Buehler, *Nanotechnology*, 2007, **18**, 295102-295110.

[3] K. Matsunaga, H. Murata, T. Mizoguchi and A. Nakahira, *Acta Biomater*. 2010, **6**, 2289–2293.

[4] L. L. Hench, *J. Am. Ceram. Soc*. 1998, **81,** 1705-1728.

[5] M. Vallet-Regí and J. M. González-Calbet, *Prog. Solid State Chem*. 2004, **32**, 1-31.

[6] S. V. Dorozhkin, *Biomatter*, 2011, **1**, 3-56.

[7] S.V. Dorozhkin. *J. Mater. Sci.*, 2007, **42**, 1061–1095.

[8] A. Bigi, G. Cojazzi, S. Panzavolta, A. Ripamonti, N. Roveri, M. Romanello, K. Noris Suarez and L. Moro. *J. Inorg. Biochem.*,1997, **68**,45–51.

[9] R. Z. LeGeros. *Calcium phosphates in oral biology and medicine*, vol. **15**. Basel: Karger; 1991, pp. 200.

[10] C. Rey, V. Renugopalakrishman, B. Collins and M.J. Glimcher, *Calcif. Tissue Int*. 1991, **49**, 251–258.

[11] J.C. Elliott, D.W. Holcomb and R.A. Young, *Calcif. Tissue Int*. 1985, **37,** 372–375.

[12] C. Rey, B. Collins, T. Goehl, I. R. Dickson and M.J. Glimcher, *Calcif. Tissue. Int.,* 1989, **45**, 157–164.

[13] R. Z. Legeros, O. R. Trautz, J.P. Legeros, E. Klein, W.P. Shirra, *Science*, 1967,**155**, 1409–1411.

[14] E. Boanini, M. Gazzano and A. Bigi, *Acta Biomater.*, 2010, **6,** 1882-1894.

[15] S. V. Dorozhkin and M. Epple, *Angew. Chem. Int. Edit.*, 2002, **41**, 3130-3146.

[16] C. Paluszkiewicz, A. Slosarczyk, D. Pijocha, M. Sitarz, M. Bucko, A. Zima, A. Chroscicka and M. Lewandowska-Szumieł. *J. Mol. Struct*., 2010, **976**, 301–309.

[17] A. Armulik, G. Svineng, K. Wennerberg, R. Faessler and S. Johansson, *Exp. Cell Res*. 2000, **254**, 55– 63.

[18] E. Gyorgy, P. Toricelli, G. Socol, M. Iliescu, I. Mayer, I. N. Mihailescu, A. Bigi and J. Werckman, *J. Biomed. Mater. Res. A*. 2004; **71**, 353-358.

[19] I. Mayer, F.J.G. Cuisinier, S. Gdalya and I. Popov. *J. Inorg. Biochem*., 2008, **102**, 311–317.

[20] L. Medvecky, R. Stulajterova, L. Parilak, J. Trpcevska, J. Durisin and S.M. Barinov. *Colloid. Surface A*, 2006, **281**, 221–229.

[21] M.B. Pabbruwe, O.C. Standard, C.H.C. Sorrell and C.R. Howlett, *Biomaterials*, 2004, **25**, 4901-4910.

[22] K. Kazuhiko, S. Hironobu, and Y. Tamoyuki, *J. Ceram. Soc. Jpn.*, 2008, **116**, 108–110.

[23] I. Sopyan and A. N. Natasha, Ionics , 2009, **15**, 735–741.

[24] I. Mayer, F.J.G. Cuisinier, I. Popov, Y. Schleich, S. Gdalya, O. Burghaus and D. Reinen, *Eur. J. Inorg. Chem*. 2006, **7**, 1460–1465.

[25] L. Lutterotti, P. Scardi and P. Maistrelli, *J. Appl. Crystallogr*., 1992, **25**, 459–462.

[26] H.M. Rietveld, *Acta Crystallogr*., 1967, **22**, 151–152.

[27] H. M. Rietveld, *J. Appl. Crystallogr*., 1969, **2**, 65–71.

[28] R.A. Young, *The Rietveld Method*, IUCr, Oxford University Press, Oxford, UK, 1993.

[29] R. A. Young and D. B. Wiles. *J. Appl. Crystallogr.*, 1982, **15**, 430–438.

[30] L. Lutterotti, Maud Version 2.26. http://www.ing.unitn.it/~maud/ (accessed 28.02.11).

[31] M. B. Hansen, S. E. Nielsen and K. Berg, *J. Immunol. Methods*, 1989, **119**, 203–210.

[32] J.P. Lafon, E. Champion and D. Bernache-Assollant, *J. Eur. Ceram. Soc.*, 2008, **28**, 139–147.

[33] A. Slosarczyk, Z. Paszkiewicz and C. Paluszkiewicz, *J. Mol. Struct.*, 2005, **744**, 657–661.

[34] L.M. de Oliveira, A.M. Rossi and R.T. Lopes, *Radiat. Phys. Chem.*, 2001, **61**, 485–487.

[35] I. Rehman and W. Bonfield, *J. Mater. Sci.-Mater. Med.*, 1997, **8**, 1-4.

[36] M. V. Chaikina, V. F. Pichugin, M. A. Surmeneva and R. A. Surmenev, *Chem. Sustain. Develop.*, 2009, **17**, 507-513.

[37] H. Ivankovic, S. Orlic, E. Tkalcec and G. Gallego Ferrer, *Kinetics of Hydroxyapatite Formation from Cuttlefish Bones*, J. G. Heinrich and C. Aneziris, Proc. 10th ECerS Conf., Göller Verlag, Baden-Baden, 2007, pp. 942-947.

[38] Q. J. He, Z. L. Huang, X. K. Cheng and J. Yu, *Mater. Lett.*, 2008, **62**, 539–542.

[39] Q. J. He, Z. L. Huang, Y. Liu, W. Chen and T. Xu, *Mater. Lett.*, 2007, **61**, 141–143.

[40] G. Suresh Kumar, E. K. Girija, A. Thamizhavel, Y. Yokogawa and S. Narayana Kalkura, *J. Colloid Interf. Sci.*, 2010, **349**, 56–62.

[41] A. Zhu, Y. Lu, Y. Si and S. Dai, *Appl. Surf. Sci.*, 2011, **257**, 3174–3179.

[42] M. H. Fathi, A. Hanifi and V. Mortazavi, *J. Mater. Process. Tech.*, 2008, **202**, 536–542.

[43] T. V. Thamaraiselvi, K. Prabakaran and S Rajeswari, *Trends Biomater. Artif. Organs*, 2006, **19**, 81-83.

[44] W. Pon-On, S. Meejoo and I.M. Tang, *Mater. Res. Bull.*, 2008, **43**, 2137– 2144.

[45] J. Terra, M. Jiang and D. E. Ellis, *Philos. Mag. A*, 2002, **82**, 2357-2377.

[46] X. Ma and D. E. Ellis, *Biomaterials*, 2008, **29**, 257–265.

[47] Y. Tang , H. F. Chappell , M. T. Dove , R. J. Reeder and Y. J. Lee, *Biomaterials*, 2009, **30**, 2864–2872.

[48] I. Mayer , G. Pető , A. Karacs, G. Molnár and I. Popov, *J. Inorg. Biochem.*, 2010, **104**, 1107–1111.

[49] M. C. Biesinger, B. P. Payne, A. P. Grosvenor, L.W.M. Lau, A. R. Gerson and R.S.C. Smart, *Appl. Surf. Sci.*, 2011,**257**, 2717–2730.

[50] H.W. Nesbitt and D. Banerjee, *Am. Mineral.*, 1998, **83**, 305–315.

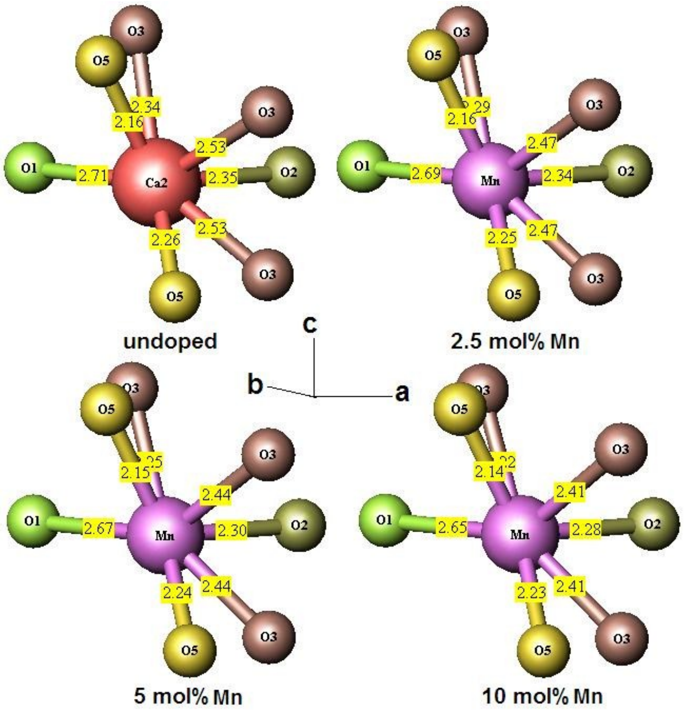

Mn substitution reduces Ca2/Mn – O bond lengths leading to structural changes in A-cHAp lattice